Weierstraß–Institut
für Angewandte Analysis und Stochastik

im Forschungsverbund Berlin e.V.

Preprint ISSN 0946 – 8633

Modeling diffusional coarsening in microelectronic solders

Wolfgang Dreyer[1], Wolfgang H. Müller[2]

submitted: March 30th 2001

[1] Weierstrass Institute
for Applied Analysis
and Stochastics
Mohrenstrasse 39
D – 10119 Berlin
Germany
E-Mail: dreyer@wias-berlin.de

[2] Department of Mechanical
and Chemical Engineering
Heriot-Watt University
Edinburgh EH14 4AS
Great Britain
E-Mail: w.h.muller@hw.ac.uk

Preprint No. 654
Berlin 2001

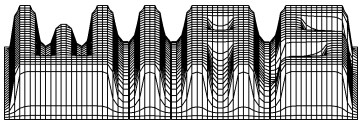

2000 *Mathematics Subject Classification.* 76R50, 82B26, 82B24, 35K30, 35K35.

Key words and phrases. Diffusion, phase transisions, interface problems, initial value problems for higher order parabolic equations, boundary value problems for higher order parabolic equations, solders, lead, tin, lead-free, coarsening, aging.

Edited by
Weierstraß–Institut für Angewandte Analysis und Stochastik (WIAS)
Mohrenstraße 39
D — 10117 Berlin
Germany

Fax: + 49 30 2044975
E-Mail (X.400): c=de;a=d400-gw;p=WIAS-BERLIN;s=preprint
E-Mail (Internet): preprint@wias-berlin.de
World Wide Web: http://www.wias-berlin.de/

Abstract

This paper presents a detailed numerical simulation of the coarsening phenomenon observed in microelectronic solder materials that are subjected to high homologeous temperatures in combination with thermo-mechanical stresses. The simulations are based on a phase field model which, for simplicity, is explicitly formulated for a binary alloy. To this end, the thermomechanical stresses originating within a Representative Volume Element (RVE) of the solder material are calculated first. This is achieved by means of a closed-form solution of the Navier equations resulting in explicit expressions for the displacements of an anisotropic, heterogeneous, thermally stressed elastic medium in discrete Fourier space. Inverse discrete Fourier transforms are then applied to these expressions in order to obtain the local stresses in real space. These in turn are inserted into an extended expression for the diffusion flux, which, in addition to the classical driving force of a concentration gradient takes the influence of different surface tensions between the solder phases as well as the local strain energy into account. The equations are evaluated numerically for the exemplary case of eutectic SnPb solder, for which all material constants are known explicitly. A comparison with aging experiments is performed.

1 Stress-assisted coarsening of microelectronic solders: Phenomenology

Solder joints that stay electro-mechanically intact are crucial for reliable long-term use of SMT packages [1], [2]. However, active use microelectronic packages results in subjecting the solder to comparatively high temperatures in combination with mechanical stresses due to thermal mismatch inherent to the structure. The resulting effect on eutectic tin-lead joints is illustrated in Figure 1 presenting a cross-sectional cut through a MELF solder joint (top) together with a cross-sectional cut through a BGA solder ball (bottom) both initially and after several thousand thermal cycles [3], [4].

The regions of different shades of gray in the solder indicate that the initially fine eutectic mix between tin and lead (SnPb) is superseded by regions of lead-rich α and tin-rich β phase. These *form and coarsen* as a consequence of diffusion among the atomic species [5], [6]. Note that the diffusion is driven by the *combined* influence of temperatures beyond 0.5 of the homologous temperature of the solder (a figure that is easily surpassed during the operation of advanced electronic packages), different

surface tensions between the two phases, and to local thermo-mechanical stresses. The latter result from thermal mismatch. More specifically, the different thermal expansion coefficients of tin and lead as well as the global thermal mismatch inherent to microelectronics structures is the cause of these stresses [4], [7], [8]. The effect of stresses becomes clearly evident by looking at Figure 1. Note that coarsening is particularly pronounced in the severely strained neck region of the BGA solder ball.

As a consequence of this phenomenon, the global material properties of the solder will change over time. Clearly, a coarsened and aged microstructure will, from a macroscopic point of view, lead to a mechanically as well as electrically destabilized and less reliable solder joint. Examples of changing *mechanical* properties include creep behavior [9], [10], decreasing yield stress [7], and ductility [11]. Moreover, for near-eutectic SnPb solders, localized coarsening accompanied by the formation of intermetallics in high stress areas precedes cracking (see the interface regions in Figure 1). It should also be noted that phase separation and coarsening as well as the associated reliability issues are by no means restricted to eutectic SnPb. The same phenomenon has experimentally already been encountered or can be expected to occur in other solders, binaries as well as ternaries, lead containing as well as lead-free. Examples of these include SnAg and SnCu, SnAgCu, SnPbAg, etc. [12]–[15].

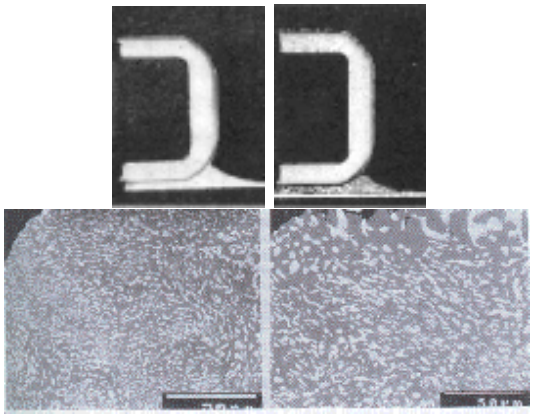

Figure 1: Cross-sectional cut through the solder joints of a MELF and a BGA.

Due to practical reasons, the tin-lead system is currently the best experimentally explored one among solders. Its industrial importance becomes evident just by looking at the immense consumption of SnPb solder in electronic equipment, which is roughly 20,000 metric tons per year world-wide [16]. Consequently, the simulations presented in this paper concentrate on SnPb for which, after some effort, all material parameters required could be obtained from the literature , i.e., from experiments that were not in any way whatsoever related to the model on which the simulations were based.

On the other hand, due to environmental reasons enforced by various legislative actions recently introduced in the U.S., the EC and in Japan [15], [17]-[19] lead-free solders become gradually more and more important. The urgency of finding thermo-

mechanically reliable substitutes which, at least, show the durability performance of the SnPb alloys is clearly imminent.

Several binary candidates have already been identified, specifically SnAu, SnAg, SnIn, SnBi, SnCu, and SnSb. Moreover, ternary and quartenary systems (SnAgCu, SnAgCuBi, SnAgCuSb) are currently being discussed [10], [11], [13], [14]. Because of the requirement for low melting and narrow freezing range coupled with an acceptable mechanical performance, these alloys are either eutectics or close to the eutectic composition and contain a substantial proportion of tin. Thus, the issues of coarsening are prone to be similar to the SnPb system.

From the microelectronics industry point of view an adequate substitute for SnPb should show good wetting behavior, be a good conductor of heat and electricity, have a similar melting point to allow continuation of the currently used reflow profiles and the to-be-joined organic materials [15]. Moreover, the new solders should be inexpensive and at least be as reliable (with regard to their mechanical properties and phase stability), easy to obtain and to process in large quantities. The following eutectics have been identified that satisfy several of these requirements: SnCu0.7 [16], [19], SnAg3.8Cu0.7 [14], SnAg3.5 [20]. It is known that SnAg shows coarsening during aging very similar to SnPb [12], [13]. Moreover, in the case of the two others Ag_3Sn and Cu_6Sn_5 intermetallics occur within a tin matrix [15]. These are reported to refine and spheroidize on aging [14]. This will clearly have some impact on their mechanical properties over time. Note that particle strengthening by intermetallic compound precipitation is a relatively new development in solders and has the potential to balance the difficulties associated with coarsening [21].

2 Stress-assisted coarsening of microelectronic solders: The experimental perspective

From an experimental point of view microstructural changes occurring during thermal cycling of solids and, in particular, in solders can already be observed using traditional *optical microscopy* provided the substructures do not become too small [22], [23].

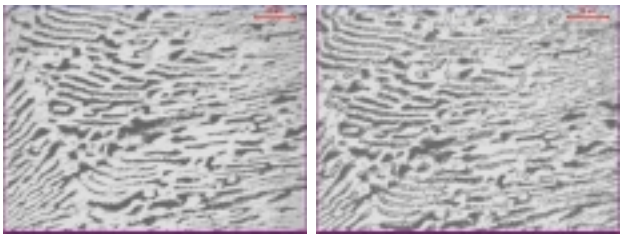

Figure 2: Near-eutectic SnPb specimen at $T = 170°$ C initially (left) and after 19 h (right) [22].

An example is presented in Figure 2 where a near-eutectic SnPb solder was exposed

to $T = 170°$ C. Due to the high homologous temperature, which for the present case is around 0.97, some coarsening could already be observed after 19h. It can be expected that an initially finer microstructure would show an even more pronounced effect [23].

In order to study coarsening more closely Electron Probe Micro Analysis (EPMA) maps can be produced on polished sections using an *Environmental Scanning Electron Microscope* (ESEM). Accurate temperature cycling regimes can be produced by the temperature control system on the ESEM stage. Information on the changes in spatial distribution of the elements as a function of temperature and time are obtained from X-ray maps. These can be produced in the form of composition, space, time matrices, which can be compared directly with the output of the numerical model described in the following section in order to determine diffusion coefficients [24]. In addition, an AFM can be used to map the topographical changes associated with grain boundary movement and precipitation of secondary phases at a resolution not available from SEM [21, 22, 25]. An example of the latter is shown in Figure 3, as well as the application of AFM techniques to lead-free solder.

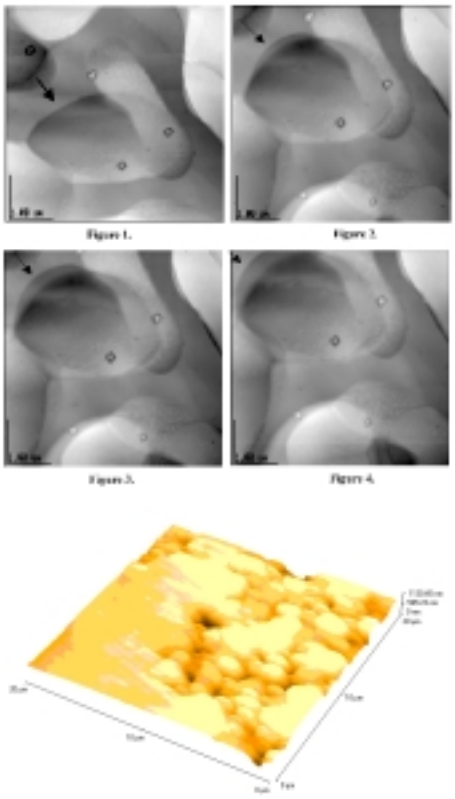

Figure 3: Growth of α-phase in 60Sn40Pb observed under the AFM [25] (first two rows) and surface topology of SnSb (courtesy R.L. Reuben, Heriot-Watt University)

3 The phase field model

The following model can effectively be used to simulate micromorphological changes in solders [3, 26, 27]. Consider a body, B, which, in the most simple case, consists of a binary alloy, i.e., SnPb, SnAg, SnCu, etc. This body is divided into representative volume elements (RVEs), which are characterized by coordinates $\underline{x} = (x_1, x_2, x_3)$ in space, and which are large enough to adequately represent the microstructure of the alloy. Within an RVE there are regions of two different phases, e.g., α and β in the case of SnPb. The α-phase has cubic material symmetry and the β-phase has tetragonal symmetry (i.e., the symmetry of the dominant elements).

From a mathematical point of view, the final objective of the model is to determine the fields of the displacement, $u_i(\underline{x}, t)$, and the field of the tin concentration, $c(\underline{x}, t) = c_{\mathrm{Sn}}(\underline{x}, t)$, for all points, $\underline{x}$, at all times, t, and at a given temperature, $T(t)$, which is supposed to be homogeneous throughout B. The assumption of a homogeneous temperature seems reasonable in view of the small amount of solder used. It is also for that reason that we refrain from solving a transient heat conduction problem and may assume the temperature to be a prescribed and known function of time. For a binary mixture, such as SnPb, only one concentration field needs to be determined since, due to mass conservation, the following identity holds:

$$c_{\mathrm{Sn}}(\underline{x}, t) + c_{\mathrm{Pb}}(\underline{x}, t) = 1, \tag{1}$$

c_{Pb} being the concentration of the second species, lead.

Moreover, it will be assumed that mechanical equilibrium is much faster to achieve than chemical equilibrium. Consequently, the mechanical part of the problem (i.e., finding $u_i(\underline{x}, t)$) will be based on the equations for static equilibrium, linear kinematic conditions and Hooke's law as follows:

$$\frac{\partial \sigma_{ij}}{\partial x_j} = 0, \quad \varepsilon_{kl} = \frac{1}{2}\left(\frac{\partial u_k}{\partial x_l} + \frac{\partial u_l}{\partial x_k}\right), \quad \sigma_{ij} = C_{ijkl}(\varepsilon_{kl} - \varepsilon^*_{kl}), \tag{2}$$

where σ_{ij} denotes the Cauchy stress tensor, ε_{kl} are the local total strains, ε^*_{kl} the nonelastic strains, such as thermal expansion, phase transformation, etc., and C_{ijkl} is the stiffness matrix which, for the time being, is assumed to be constant in space. For a suitable initial condition (see below), to be prescribed within the heterogenous RVE, the fields of the displacements, u_k, can be computed in discrete Fourier space, based on a formalism suggested before [28, 29]. To this end consider an array of N discrete points, $\underline{\alpha}$, arranged equidistantly across a square RVE of dimension d and of side length $2\pi L$: Figure 4. Periodicity conditions are assumed to hold across the RVE and by mutual insertion of the equations shown in (1) and by application of Discrete Fourier Transforms (DFT) [3], [28]–[31] the following formal solution is obtained:

$$\begin{aligned} \hat{\varepsilon}_{ij}(\underline{s}) &= \hat{A}_{ijkl}(\underline{s})\hat{\varepsilon}^*_{kl}(\underline{s}) + \hat{\varepsilon}^0_{ij}(\underline{s}), \qquad (3) \\ \hat{A}_{ijkl} &= \begin{cases} 0, \underline{s} = \underline{0} \\ \frac{1}{2D}(\xi_i N_{js} + \xi_j N_{is}) C_{srkl} \xi_r, \underline{s} \neq \underline{0} \end{cases}, \end{aligned}$$

where $\underline{s}$ is the discrete position vector in Fourier space.

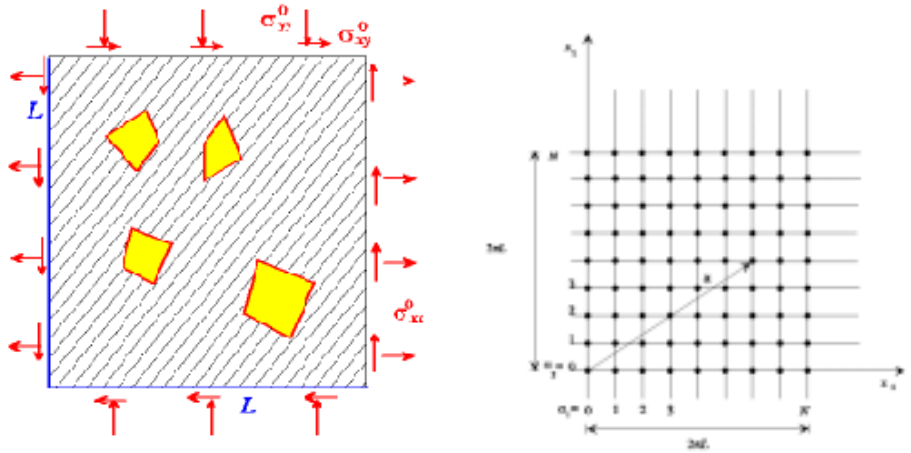

Figure 4: Square RVE (top) and its discretization (bottom) in 2D for $N = 8$

The symbols N_{js} and D are cumbersome but known functions of the stiffness, C_{ijkl}, and of the Fourier transforms of difference quotients, ξ_i, which were used for an approximate solution of the extended Navier system of PDEs that follows from Eqns. (2) [32].

Loading of the body is taken into account in two ways. First, it can result from different thermal expansion coefficients of the two phases:

$$\begin{aligned} \varepsilon^*_{kl}(\underline{x},t) &= \alpha_{kl}(\underline{x},t)\cdot(T-T_R), \\ \alpha_{kl}(\underline{x},t) &= \theta(\underline{x},t)\alpha^{\alpha}_{kl} + (1-\theta(\underline{x},t))\alpha^{\beta}_{kl}, \\ \theta(\underline{x},t) &= \frac{c_\beta - c(\underline{x},t)}{c_\beta - c_\alpha} \Rightarrow \theta(\underline{x},t) = \begin{cases} 0 & \underline{x}=\beta \\ \text{if} & \\ 1 & \underline{x}=\alpha \end{cases}, \end{aligned} \tag{4}$$

where T_R is the reference temperature of the stress-free state (i.e., the solidus temperature of the solder). The symbols α^{α}_{ij} and α^{β}_{ij} are tensors of thermal expansion coefficients of the cubic α and of the tetragonal β-phase, respectively, which for the binaries mentioned take the following form with respect to the crystallographic coordinate system:

$$\alpha^{\alpha}_{ij} = \begin{pmatrix} \alpha^{\alpha} & 0 & 0 \\ 0 & \alpha^{\alpha} & 0 \\ 0 & 0 & \alpha^{\alpha} \end{pmatrix}, \qquad \alpha^{\beta}_{ij} = \begin{pmatrix} \alpha^{\beta}_1 & 0 & 0 \\ 0 & \alpha^{\beta}_1 & 0 \\ 0 & 0 & \alpha^{\beta}_3 \end{pmatrix}. \tag{5}$$

To a first order approximation the elements of these matrices are given by the thermal expansion coefficients of the *pure* species (i.e., lead and tin in the case of SnPb). In order to account for higher order terms Vegard's law [33] or rules of mixtures can be used to relate them to the thermal expansion coefficients of the pure

materials. For obvious reasons $\theta(\underline{x},t)$ is known as the *shape function* and requires the equilibrium concentrations of the α and of the β -phase, c_α and c_β, as input. For a given temperature these are constant and can be read off from a phase diagram or obtained from a thermodynamics database [34]. This way the eigenstrains are directly connected to the *current local* composition of the alloy, which guarantees a *continuous* transition between the regions. Initially a suitable function of position will be assumed for $c(\underline{x},t)$ (e.g., local tin-rich nuclei), which results in an initial condition for the eigenstrains ε^*_{kl}.

Second, loading can be also imposed from outside by prescribing suitable mean averages for the strains over the RVE, ε^0_{ij} [35]. Physically speaking, these are due to the global thermal mismatch of the microelectronic structure. Consider now the case of a spatially varying stiffness matrix:

$$C_{ijkl}(\underline{x},t) = \theta(\underline{x},t)C^\alpha_{ijkl} + (1-\theta(\underline{x},t))C^\beta_{ijkl}. \tag{6}$$

In this equation C^α_{ijkl} and C^β_{ijkl} are the elements of the stiffness matrix of the α and of the β-phase, respectively, which are assumed to be constant and known quantities. In Voigt's notation they can be obtained from the following matrix schemes:

$^{kl}_{ij}$	11	22	33	23	31	12
11	C^α_{11}	C^α_{12}	C^α_{12}	0	0	0
22	C^α_{12}	C^α_{11}	C^α_{12}	0	0	0
33	C^α_{12}	C^α_{12}	C^α_{11}	0	0	0
23	0	0	0	C^α_{44}	0	0
31	0	0	0	0	C^α_{44}	0
12	0	0	0	0	0	C^α_{44}

$^{kl}_{ij}$	11	22	33	23	31	12
11	C^β_{11}	C^β_{12}	C^β_{13}	0	0	0
22	C^β_{12}	C^β_{11}	C^β_{13}	0	0	0
33	C^β_{13}	C^β_{13}	C^β_{33}	0	0	0
23	0	0	0	C^β_{44}	0	0
31	0	0	0	0	C^β_{44}	0
12	0	0	0	0	0	C^β_{66}

(7)

Now the Equivalent Inclusion Method (EIM) [32] is used [30, 36, 37] in order to determine the stress/strain fields iteratively from an auxiliary discrete strain field $\varepsilon^{\max}_{kl}(\underline{\alpha})$:

$$\begin{aligned}
&\sigma_{ij}(\underline{\alpha}) = C_{ijkl}(\underline{\alpha},t)(\varepsilon_{kl}(\underline{\alpha}) - \varepsilon^*_{kl}(\underline{\alpha})) = C^{aux}_{ijkl}(\varepsilon_{kl}(\underline{\alpha}) - \varepsilon^*_{kl}(\underline{\alpha}) - \varepsilon^{aux}_{kl}(\underline{\alpha})),\\
&\varepsilon_{kl}(\underline{\alpha}) = Y^{-1}\left[\hat{A}^{aux}_{klop}\hat{\varepsilon}^*_{op}\right] + Y^{-1}\left[\hat{A}^{aux}_{klop}\hat{\varepsilon}^{aux}_{op}\right] + \varepsilon^0_{kl}.
\end{aligned} \tag{8}$$

In order to always guarantee convergence the spatially constant stiffness tensor, C^{aux}_{ijkl}, can be chosen as $C^{aux}_{ijkl} = 0.5(C^\alpha_{ijkl} + C^\beta_{ijkl})$ [38]. If the second relation shown in Eqn (8) is inserted into the first one and Eqn (6) is observed then the following Neumann iteration procedure for the unknown field ε^{aux}_{kl} is obtained:

$$\begin{aligned}
&\overset{(n+1)}{\varepsilon}{}^{aux}_{kl} = (C^{aux})^{-1}_{klrs}\left(C^{aux}_{rsmn} - C^\beta_{rsmn} - \theta(\underline{\alpha})[C^\alpha_{rsmn} - C^\beta_{rsmn}]\right) \times\\
&\left(\varepsilon^0_{mn} + Y^{-1}\left[\hat{A}^{aux}_{mnop}\hat{\varepsilon}^*_{op}\right] + Y^{-1}\left[\hat{A}^{aux}_{mnop}\overset{(n)}{\hat{\varepsilon}}{}^{aux}_{op}\right] - \varepsilon^*_{mn}\right), \overset{(0)}{\varepsilon}{}^{aux}_{op} = 0.
\end{aligned} \tag{9}$$

Y^{-1} denotes the inverse discrete Fourier transform and the symbols $\hat{A}^{aux}_{mnop}$ can be computed from $\hat{A}_{mnop}$ (cf., Eqn. (3)) if C_{ijkl} is substituted by C^{aux}_{ijkl}. In fact, EIM was originally developed for the continuum and Eqn. (9) is the discrete counterpart of the standard Neumann iteration technique for the solution of a Fredholm integral equation for the continuous field $\varepsilon^{aux}_{kl}(\underline{x})$.

Once the strains and stresses are known at a certain time, t, they will be used to compute the temporal evolution of the distribution of concentrations, c, during the next time-step, Δt. The calculation is based on a numerical solution of the following PDE [3], [26]–[28], [30]:

$$\frac{\partial c}{\partial t} + \frac{\partial J_i}{\partial x_i} = 0, \tag{10}$$

$$J_i = -M_{ij}\frac{\partial}{\partial x_j}\left(\underline{\frac{\partial \psi}{\partial c}} - \underline{\underline{a_{kl}\frac{\partial^2 c}{\partial x_k \partial x_l}}} + \frac{1}{2}\frac{\partial}{\partial c}\left[\sigma_{kl}(\varepsilon_{kl} - \varepsilon^*_{kl})\right]\right)$$

where M_{ij} is the matrix of mobility coefficients that, as in the case of Eqns. (4, 6), is connected to the mobility coefficients of the α and of the β-phase as follows: $M_{ij}(\underline{x}, t) = \theta(\underline{x}, t)M^{\alpha}_{ij} + (1 - \theta(\underline{x}, t))M^{\beta}_{ij}$. Moreover, ψ is the configurational part of the Gibbs free energy density of the system. Following general practice, the Gibbs free energy densities of the two phases α/β of a binary system A/B are decomposed into three additive parts. First, a contribution accounting for the free energies of the pure components, $g^{\alpha/\beta}_A$, $g^{\alpha/\beta}_B$, second a logarithmic part due to the entropy of mixture and, third, the heat of mixture term acknowledging the fact that the mixture is non-ideal:

$$g^{\alpha/\beta} = y g^{\alpha/\beta}_A + (1-y) g^{\alpha/\beta}_B + R\,T\Big[y\ln(y) + (1-y)\ln(1-y)\Big] + y(1-y) l^{\alpha/\beta}_{A,B}. \tag{11}$$

The choice of variables follows the convention employed by MTDataő [34], i.e., the Gibbs free energy shown in Eqn. (11) is provided in units of J/mol as a function of particle concentration, y, and needs to be rewritten suitably before it can be inserted into Eqn. (10) [26, 27]. The coefficients $g^{\alpha/\beta}_A$, $g^{\alpha/\beta}_B$, $l^{\alpha/\beta}_{A,B}$ depend on absolute temperature, T:

$$\begin{aligned} g^i_j &= A^i_j + B^i_j T + C^i_j T\ln(T) + D^i_j T^2 + E^i_j T^3 + \frac{F^i_j}{T}, \qquad i \in \{\alpha,\beta\},\ j \in \{A,B\}, \\ l^i_{A,B} &= A^i + B^i T, \qquad i \in \{\alpha,\beta\}. \end{aligned} \tag{12}$$

The remaining coefficients are tabulated [34]. For the transformation into units of $\mathrm{J/m^3}$ and mass concentrations the following relations apply:

$$\begin{aligned} y &= \frac{M^B c}{M^A - c(M^A - M^B)}, \quad M = \frac{M^A M^B}{M^A - c(M^A - M^B)}, \\ \psi^{\alpha/\beta} &= \frac{g^{\alpha/\beta}(c(y))}{M(c)} \cdot 10^3 \frac{\mathrm{mol}}{\mathrm{kg}} \rho \end{aligned} \tag{13}$$

M^A and M^B being the molecular weights of the two species, and ρ being the mass density of the binary alloy.

It should be noted that the single underlined term in Eqn. (10) corresponds to classical diffusion theory as proposed by Fick, whereas the double underlined part contains extensions as introduced by Cahn and Hilliard, a_{ij}representing matrices of surface tensions of both phases [39]:

$$a_{ij}(\underline{x},t) = \theta(\underline{x},t)a_{ij}^{\alpha} + (1-\theta(\underline{x},t))a_{ij}^{\beta}. \tag{14}$$

Moreover, Eqn. (10) contains a third term that characterises the influence of mechanical deformation energy on the diffusion process: $\frac{1}{2}\frac{\partial}{\partial c}\left[\sigma_{kl}(\varepsilon_{kl}-\varepsilon_{kl}^{*})\right]$ [3], [40]-[43]. The numerically calculated change in concentrations during the time Δt will lead to a change of the micromorphology and, consequently, necessitates an update of the local stress / strain distribution in the RVE by means of Eqns. (8, 9). If this has been achieved, the next time-step is considered. Details of the numerical strategies involved (solution by means of DFT using a partially implicit Euler scheme) can be found in the literature [3, 27]. The evolution will be illustrated in one of the following sections.

4 A summary of relevant material parameters and the initial condition

In what follows we present numerical values for all material parameters required by the model. This will specifically be done for the exemplary case of SnPb. Note that *no* fit of the parameters was performed in order to achieve a "better" agreement with experimental observations. It should be pointed out that all parameters are physically motivated and stem from experiments that are completely unrelated to the present model.

Mobilities This data is based on diffusion coefficients for tin or lead being a tracer element in pure lead and tin, respectively [3]. Clearly, the diffusion coefficient for the α phase is much smaller than the one for the β phase and can be neglected in the quantitative simulations:

$$\begin{aligned}
125^{\circ}\mathrm{C}: \quad M^{\alpha}\Big|_{c^{\alpha}} &= 2.42\cdot 10^{-27}\frac{\mathrm{m}^5}{\mathrm{Js}}, \\
M_1^{\beta}\Big|_{c^{\beta}} &= 4.52\cdot 10^{-24}\frac{\mathrm{m}^5}{\mathrm{Js}}, \\
20^{\circ}\mathrm{C}: \quad M^{\alpha}\Big|_{c^{\alpha}} &= 1.27\cdot 10^{-32}\frac{\mathrm{m}^5}{\mathrm{Js}}, \\
M_1^{\beta}\Big|_{c^{\beta}} &= 1.11\cdot 10^{-27}\frac{\mathrm{m}^5}{\mathrm{Js}}.
\end{aligned} \tag{15}$$

Gibbs Free Energy MTdata provides the following information for the system SnPb regarding the parameters shown in Eqn. (11):

	A_j^i $\left[\frac{\text{kJ}}{\text{mol}}\right]$	B_j^i $\left[\frac{\text{J}}{\text{molK}}\right]$	C_j^i $\left[\frac{\text{J}}{\text{molK}}\right]$	D_j^i $\left[\frac{\text{mJ}}{\text{molK}^2}\right]$	E_j^i $\left[\frac{\mu\text{J}}{\text{molK}^3}\right]$	F_j^i $\left[\frac{\text{MJK}}{\text{mol}}\right]$
$i = \alpha$						
$j = \text{Pb}$	−7.650	101.7002	−24.5242	−3.659	−0.244	0
$j = \text{Sn}$	−1.705	60.24332	−15.9610	−18.870	3.12117	−0.062
$i = \beta$						
$j = \text{Pb}$	−7.161	105.2202	$= C^{\alpha}_{\text{Pb}}$	$= D^{\alpha}_{\text{Pb}}$	$= E^{\alpha}_{\text{Pb}}$	$= F^{\alpha}_{\text{Pb}}$
$j = \text{Sn}$	−5.855	65.44332	$= C^{\alpha}_{\text{Sn}}$	$= D^{\alpha}_{\text{Sn}}$	$= E^{\alpha}_{\text{Sn}}$	$= F^{\alpha}_{\text{Sn}}$

and:

	A^i $\left[\frac{\text{kJ}}{\text{mol}}\right]$	B^i $\left[\frac{\text{J}}{\text{mol}}\right]$
$i = \alpha$	5.13241	1.56312
$i = \beta$	17.11778	-11.80656

Using these parameters leads to Figure 5, which shows typical Gibbs free energy curves for two different temperatures. The common tangent construction (Maxwell lines) is demonstrated in the figure resulting in the two equilibrium concentrations c_α and c_β (outermost bullet points) mentioned above. The figure also contains the spinodal points (innermost bullet points) that form the boundary of the non-convex unstable region of concentrations.

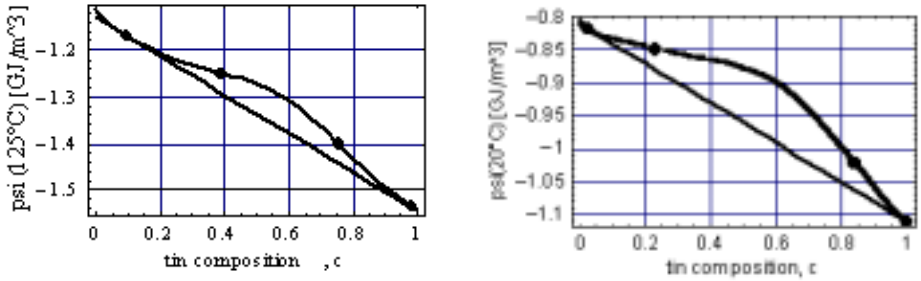

Figure 5: Gibbs free energies at 125° C and 20° C including Maxwell and spinodal points [34].

Surface Tensions For the microstructural development in SnPb the surface tension terms according to Cahn-Hilliard are of greatest importance. A study of the atomic potentials and lattice configurations allows to conclude that [3, 27]:

$$a_{kl}^{\alpha} = a^{\alpha}\delta_{ij}, \quad a^{\alpha} = 1.5 \cdot a, \quad a_{kl}^{\alpha} = \begin{pmatrix} a & 0 & 0 \\ 0 & a & 0 \\ 0 & 0 & 14a \end{pmatrix}, \tag{16}$$
$$a = \frac{2\gamma\Delta x}{(c^{\beta} - c^{\alpha})^2}, \quad \gamma = 1.5\frac{\mathrm{J}}{\mathrm{m}^2}, \quad \Delta x = 25\mathrm{nm}.$$

It should be noted that the strong anisotropy of the surface tensions and not the mobility matrices will lead to the development of directed structures, i.e., eutectic *lamellae* shown in the simulations.

Eigenstrains For the eigenstrains arising in SnPb, which are incoherent in nature, we write [3, 27]:

$$\begin{aligned} \varepsilon_{kl}^{*} &= \alpha_{kl}(\underline{x}, t) \cdot \Delta T, \qquad \Delta T = (T - T_R), \\ \alpha_{kl} &= \theta(\underline{x}, t)\alpha_{kl}^{\alpha} + (1 - \theta(\underline{x}, t))\alpha_{kl}^{\beta}, \end{aligned} \tag{17}$$

where:

$$\alpha^{\alpha} = 28.9 \cdot 10^{-6}\mathrm{K}^{-1}, \quad \alpha_1^{\alpha} = 16.7 \cdot 10^{-6}\mathrm{K}^{-1}, \quad \alpha_3^{\beta} = 36.4 \cdot 10^{-6}\mathrm{K}^{-1}. \tag{18}$$

Stiffnesses Mechanical data for pure tin and lead are easy to obtain and will be used to approximate the stiffnesses of the two phases [3, 27]:

$$\begin{aligned} &C_{11}^{\alpha} = 49.66 \text{ GPa}, \quad C_{12}^{\alpha} = 42.31 \text{ GPa}, \quad C_{44}^{\alpha} = 14.98 \text{ GPa}, \\ &C_{11}^{\beta} = 75.29 \text{ GPa}, \quad C_{12}^{\beta} = 61.56 \text{ GPa}, \quad C_{13}^{\beta} = 44.00 \text{ GPa}, \\ &C_{33}^{\beta} = 95.52 \text{ GPa}, \quad C_{44}^{\beta} = 21.93 \text{ GPa}, \quad C_{66}^{\beta} = 23.36 \text{ GPa}. \end{aligned} \tag{19}$$

Eutectic SnPb All simulations of the phase separation and coarsening in SnPb solder were based on the initial condition plotted in Fig. 10 across an RVE of resolution 128 $\times$ 128 (RVE side length: $2\pi L = 1\mu$m). Note that we start from an essentially homogeneous concentration profile at the eutectic level with a few small fluctuations: Figure 6. As it was mentioned above the eutectic concentration is highly unstable since it falls in between the spinodal points shown in Fig. 5, i.e., within the unstable convex region of the Gibbs free energy curve. Consequently spinodal decomposition into the two phases will occur at the slightest fluctuation.

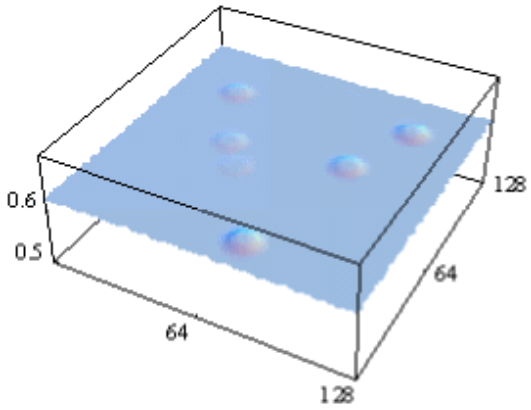

Figure 6: The initial condition used for SnPb simulations: a uniform eutectic concentration with a few fluctuations

5 Numerical simulations and comparison to the experiment

The following simulations were performed for an inclination of 25° between the crystallographic and the laboratory system. The size of the RVEs shown is $2\pi L = 1\mu$m. Figure 7 shows a comparison of the microstructural development at two different temperatures, 20°C and 125°C, respectively. Note that the equilibrium volume fractions of the two phases at these two temperatures are slightly different. However, what is more important is that the time scales involved in coarsening at the two temperatures are of a different order of magnitude. To a certain degree this is in agreement with experimental observations presented in Figure 8 [45]. Naturally, the quantitative agreement is not perfect yet. This is due to the values of the mobility coefficients listed above which, as it was mentioned, stem from tracer experiments and do *not* perfectly reflect the present situation. However, the general trend has already been captured.

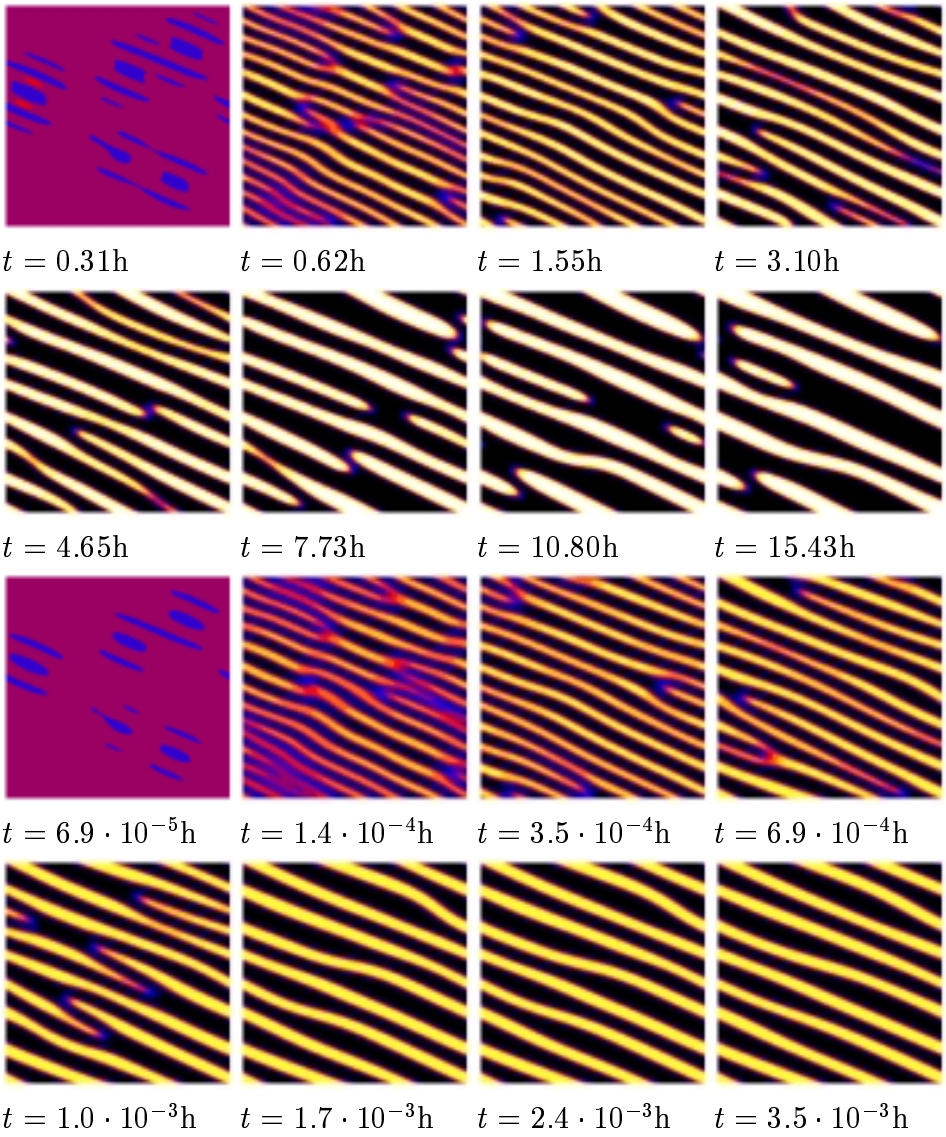

Figure 7: Low temperature (first two rows) vs. high temperature (last two rows) development

The sequences of pictures shown in Figures 9-11 explore the influence of tensile stress on microstructural development. Summarizing we may say that both *uniaxial tensions* in horizontal as well as in vertical direction lead to clearly visible coarsening behavior. Consequently, such a state of stress may be considered to contribute to the pronounced coarsening occurring in the neck regions of solder balls (cf., Figure 1). Clearly, the state of stress in that case is three-dimensional in nature but in can be anticipated that the principal stresses are *not* all equal. It turns out that *equal* tensile loads lead to hardly any coarsening at all. The corresponding results are presented in the sequence of pictures shown in Figure 11. Judging by these simulations it can be claimed that the effects of two tensile loads of equal size on the microstructure seem to annihilate each other although, during the development, some differences

to the corresponding structures without external loads (Figure 7) can be observed.

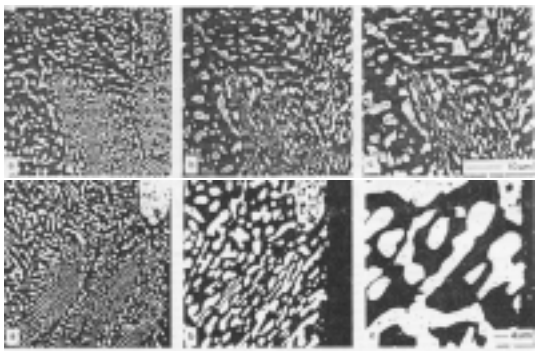

Figure 8: Experimental investigation of the influence of temperature on microstructural coarsening in eutectic SnPb, first row aging at after (a) 2 hours, (b) 17 days, and (c) 63 days after solidification; second row: aging at 125°C (a) immediately after solidification, (b) after 3 hours at and (c) 300 hours [45]

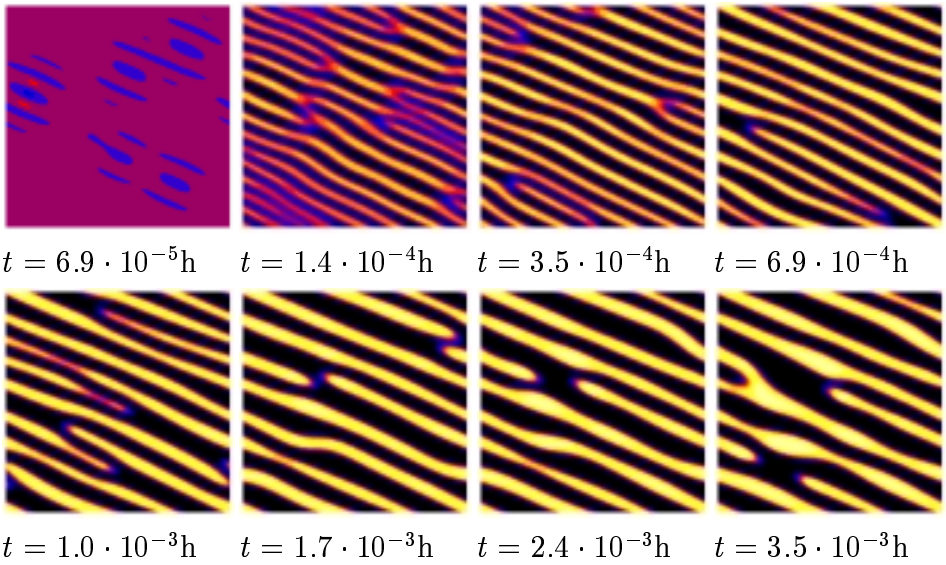

Figure 9: High temperature development, external load of +5MPa in horizontal direction

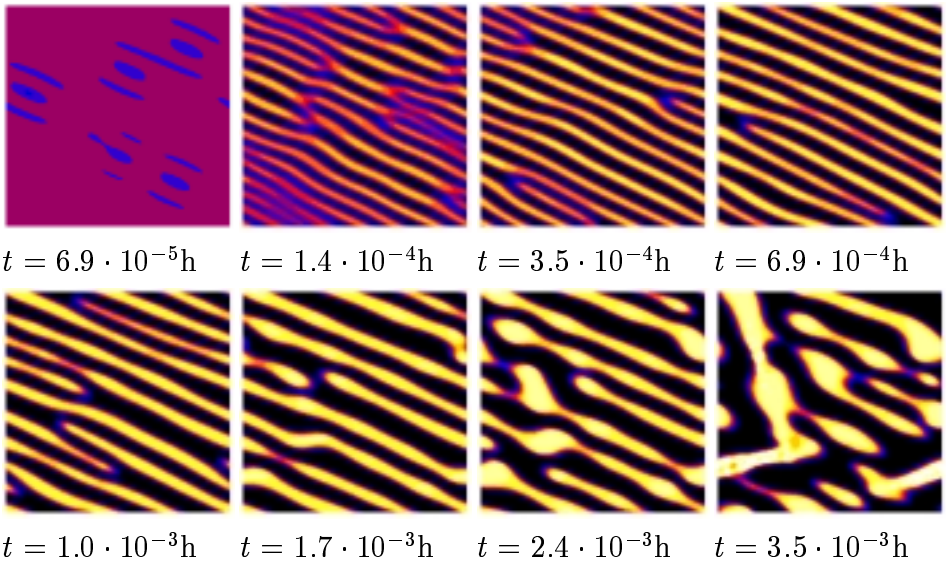

Figure 10: High temperature development, external load of +5MPa in vertical direction

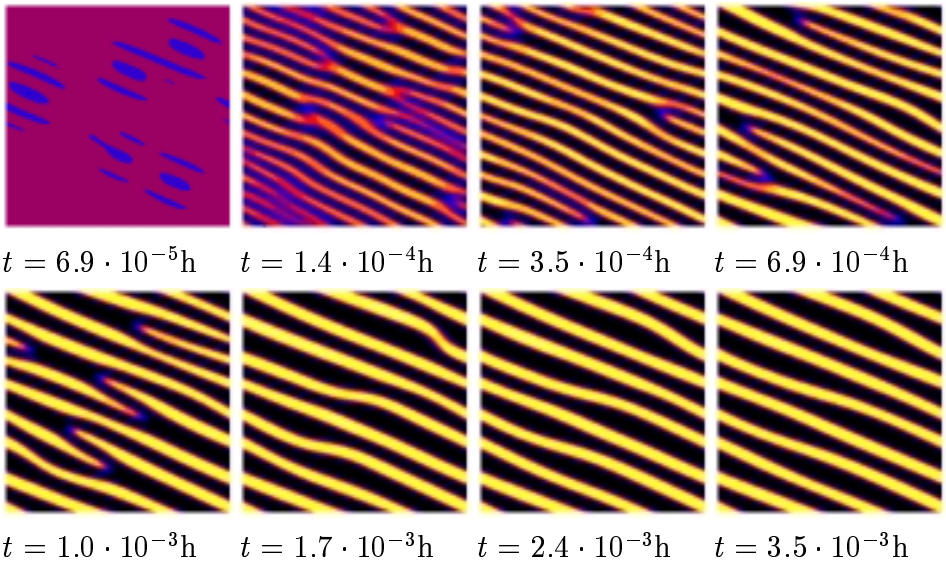

Figure 11: High temperature development, external load of +5MPa in both directions

Figures 12 and 13 investigate the impact of compressive uniaxial stresses in horizontal and in vertical direction, respectively. We may say that the microstructures resulting under these states of stress are very similar to their tensile counterparts shown in Figure 9 and 10. However, tensile stresses seem to have a slightly stronger coarsening effect.

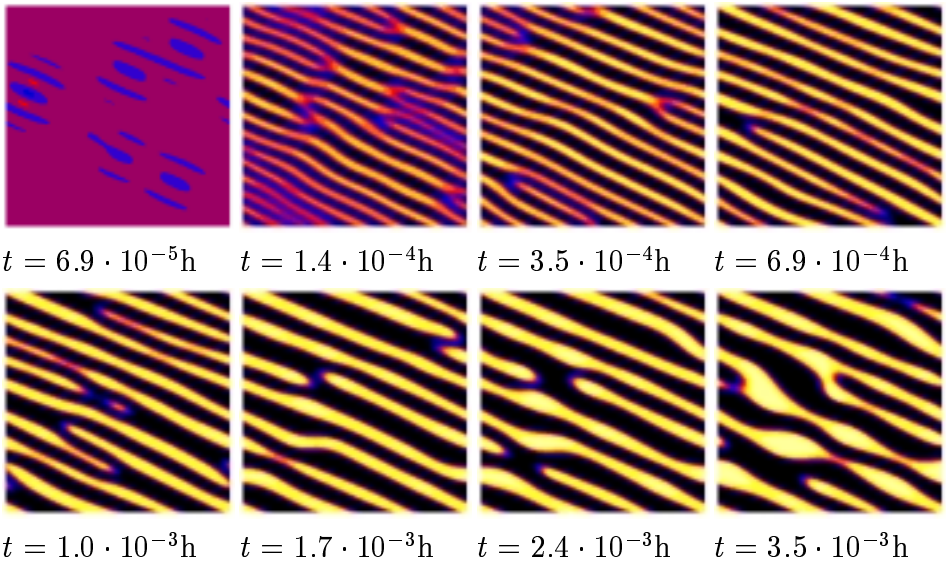

Figure 12: High temperature development, external load of -5MPa in horizontal direction

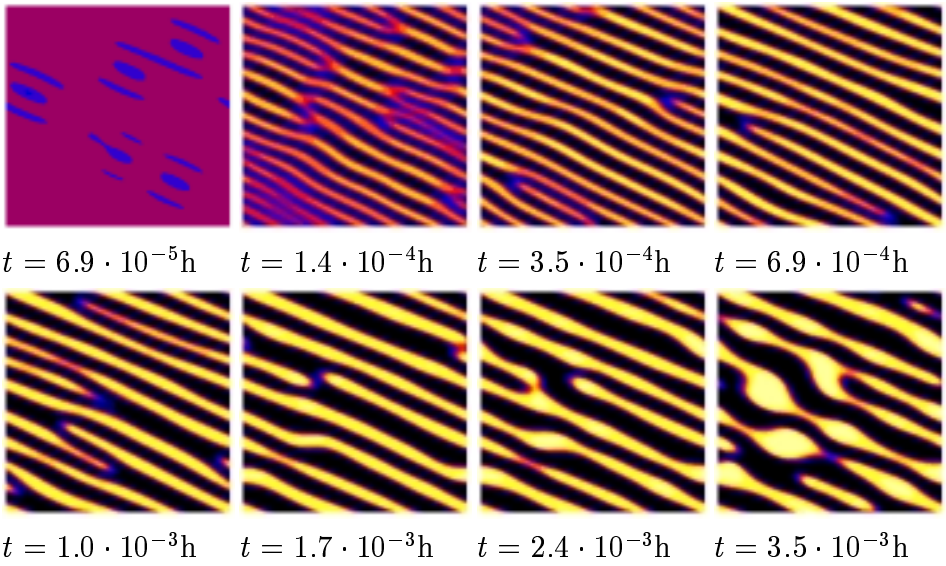

Figure 13: High temperature development, external load of -5MPa in vertical direction

Figure 14 and 15 focus on the effect of shear stress applied to an RVE. Obviously, if the shear stress is sufficiently high, i.e., of the same magnitude 5MPa as the tensile and the compressive stresses above, its effect can be dramatic (cf., Figure 14). Reducing the shear by more than 50% still leads to a noticeable effect during the development phase. However, eventually the microstructure looks similar when compared to the sequence with no external load shown in Figure 7.

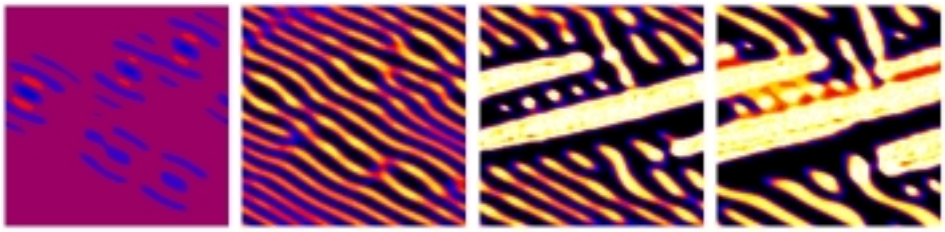

$t = 6.9 \cdot 10^{-5}\text{h}$ $t = 1.4 \cdot 10^{-4}\text{h}$ $t = 3.5 \cdot 10^{-4}\text{h}$ $t = 6.9 \cdot 10^{-4}\text{h}$

Figure 14: High temperature development, -5MPa shear

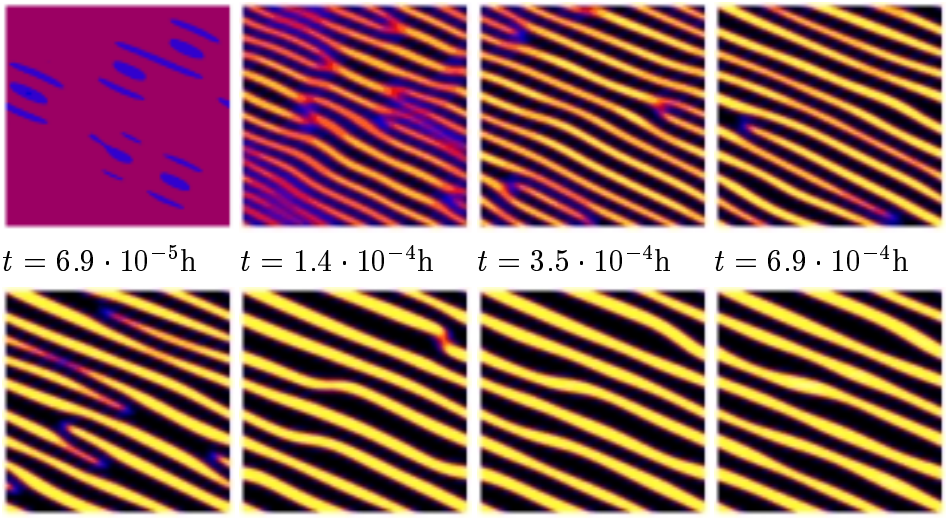

$t = 6.9 \cdot 10^{-5}\text{h}$ $t = 1.4 \cdot 10^{-4}\text{h}$ $t = 3.5 \cdot 10^{-4}\text{h}$ $t = 6.9 \cdot 10^{-4}\text{h}$

$t = 1.0 \cdot 10^{-3}\text{h}$ $t = 1.7 \cdot 10^{-3}\text{h}$ $t = 2.4 \cdot 10^{-3}\text{h}$ $t = 3.5 \cdot 10^{-3}\text{h}$

Figure 15: High temperature development, -2MPa shear

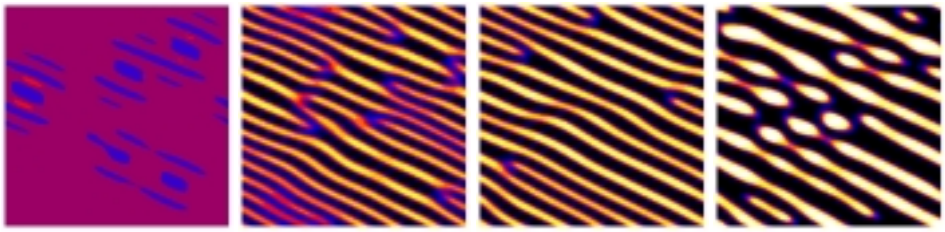

$t = 6.9 \cdot 10^{-5}\text{h}$ $t = 1.4 \cdot 10^{-4}\text{h}$ $t = 3.5 \cdot 10^{-4}\text{h}$ $t = 6.9 \cdot 10^{-4}\text{h}$

Figure 16: Low temperature development, external load of 5MPa in vertical direction

The sequence of Figure 16 demonstrates that coarsening due to external loads is by no means restricted to high temperatures. Rather it will occur at room temperature as well albeit with a different intensity.

Finally the sequence of Figure 17 provides evidence that there is potential for "healing" of a coarsened microstructure. For this simulation the last picture shown in Figure 13 served as initial condition to further simulations of the microstructural

development at room temperature after the external stress had been switched off. At this point it should be mentioned that the ever-present thermal mismatch between the two phases does not have a visible impact on coarsening at least in the case of the SnPb system. Due to the fact that equilibrium concentrations and phase volume fractions depend on temperature, diffusion sets in, which obviously has a smoothening effect on the microstructure.

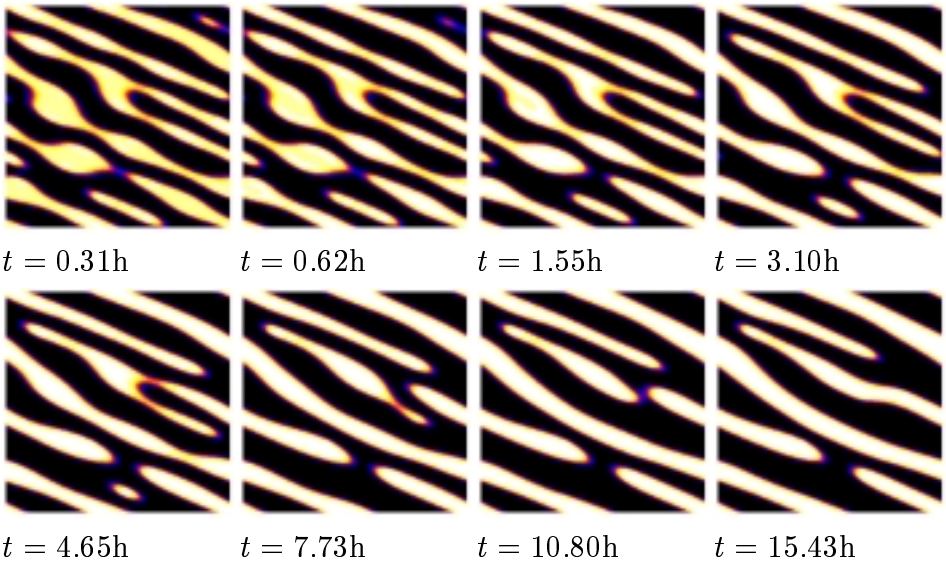

Fiure 17: "Healing" of a coarsened microstructure by switching to a different temperature 125°C→ 20°C.

6 Conclusions and outlook

The following conclusions can be drawn:

- Coarsening of eutectic SnPb with or without external loads and at different temperatures can be simulated quantitatively. For this alloy all material coefficients are known with sufficient accuracy. The results are in reasonable agreement with experimental investigations. In order to further improve the results microscopic in-situ observations should be performed, which in combination with computer simulations could help to improve our knowledge on the mobility coefficients. First computer simulations seem to indicate that there is potential for healing a coarsened structure by suitable thermal management. This has to be validated by suitably arranged experiments.

- The theoretical techniques to study coarsening phenomena in binary lead-free solders are available and ready for evaluation provided all required material parameters can be obtained. This seems feasible, at least for alloys systems, such as SnCu or SnAg.

- In order to simulate coarsening in ternary or even higher solder alloys the presented theory needs to be extended suitably. Investigations are currently underway by the authors to provide the required framework.

References

[1] Lau, J.H., Rice, D.W., *Solder joint fatigue in surface mount technology: State of the art*, Solid State Technology, 1985, pp. 91–104.

[2] Frear, D.R., Morgan, H.S., Burchett, S. IV., Lau, J., *The mechanics of solder alloy interconnects*, Van Nostrand Reinhold, New York, 1993.

[3] Dreyer, W., Müller, W.H., *A study of the coarsening in tin/lead solders*, Internat. J. Solids Structures **37** (2000), No. 28, pp. 3841–3871.

[4] Nylén, M., Hutchinson, B., Gustavsson, U., *Microstructural degradation of solder*, Proc. Micro Materials, Micro Mat '97, Berlin, 1997, pp. 890–895.

[5] Ozmat, B., *A nonlinear thermal stress analysis of surface mount solder joints*, Proc. 40th IEEE ECTC, Vol. II, 1990, pp. 959–972.

[6] Pao, Y.-H., *A fracture mechanics approach to thermal fatigue life prediction of solder joints*, IEEE Transactions on Components, Hybrids, and Manufacturing Technology, 1992, 15 (4), pp. 559–570.

[7] Seyyedi, J., Arsenault, B., Keller, J.P., *Stress-rupture and creep behaviour of 63Sn-37Pb production soldered connections*, Soldering & Surface Mount Technology, 1991, 7, pp.49–55.

[8] Dudek, R., Nylén, M., Schubert, A., Michel, B., Reichl, H., *An efficient approach to predict solder fatigue life and its application to SM- and area-array components*, In: Materials Mechanics, Fracture Mechanics, Micro Mechanics (T. Winkler, A. Schubert, editors). Berlin, 1999, pp. 365–374.

[9] Darveaux, R., Banerji, K., Mawer, A., Dody, G., *Reliability of plastic ball grid array assembly*, Ball Grid Array Technology, (J. H. Lau). SMTnet, 1995, pp. 380–442.

[10] Lee, N.-C., *Getting ready for lead-free solders*, Soldering and Surface Mount Technology, 1997, 26, pp. 65–69.

[11] Nguyen, v.S., Herrmann, K.P., Müller, W.H., Albrecht, H.-J., Foulds J., *Determination of mechanical parameters of solder materials using the miniature measuring method "small punch test"*, Proc. MicroMat 2000, Berlin, 2000, pp. 671–674.

[12] Chada, S., Herrmann, A., Laub, W., Fournelle, R., Shangguan, D., Achari, A., *Microstructural investigation of Sn-Ag and Sn-Pb-Ag solder joints*, Soldering & Surface Mount Technology, 1997, 26, pp. 9–21.

[13] Lord, P.C., Witt, M.C., Bilham, R., Edwards, T., Ling, C., *Rating lead-free BGA solder alloys*, SMT, 1997 pp. 86–89.

[14] Warwick, M., *Implementing lead free soldering – European consortium research*, Journal of SMT, 1999, 12 (4), pp. 1–12.

[15] Abtew, M., Selvaduray, G., *Lead-free solders in microelectronics*, Materials Science and Engineering Reports, 2000, 27, pp. 95–141.

[16] Trumble, B., *Get the lead out!*, IEEE Spectrum, 1998, pp. 55–60.

[17] Low, M.K., Williams, D.J., *European environmental legislation in electronics and its potential impact on Far Eastern suppliers*, Proc. EPTC '98, Singapore, 8-10 December, 1998, IEEE, Piscataway, NJ., pp. 206–213.

[18] Lau, J.H., Chang, C., *TMA, DMA, DSC and TGA of lead free solders*, Soldering & Surface Mount Technology, 1999, 11/2, pp. 17–24.

[19] Miric, A.Z., *Bleifreie Lotlegierungen* (Lead free solder alloys), VTE, 1999, 11 (5), pp. 259–269.

[20] Adolphi, B., *Bleifreie Lote - und was nun?* (Lead free solders and now what?), VTE, 1999, 11 (5), pp. 238–245.

[21] Yassin, A., Reuben R.L., Saad, G., Beshai, M.H.N., Habib, S.K., *Effect of annealing and microstructure on the creep behaviour of an Sn-10% Sb alloy,* Proc. of the Institution of Mechanical Engineers Part L - Journal of Materials-Design and Applications, 1999, 213 (L1), pp. 59–68.

[22] Foltyn, T., *The effect of coarsening on near eutectic lead-tin alloy*, MSc thesis, Department of Mechanical and Chemical Engineering, Heriot-Watt University, 2000.

[23] Vianco, P.T., Burchett, S.N., Neilsen, M.K., Rejent J. A., Frear, D. R., *Coarsening of the Sn-Pb solder microstructure in constitutive model-based predictions of solder joint thermal mechanical fatigue*, Journal of Electronic Materials, 1999, 28 (11), pp. 1290–1298.

[24] Johnson, R., *Environmental Scanning Electron Microscopy, An Introduction to ESEM*, Philips Electron Optics, Eindhoven, The Netherlands, 2nd printing, 1996.

[25] Leonard, D.N., Russel, P.E., *Using a moderate vacuum, hot/cryo-stage equipped AFM for in-situ observation of α-phase growth in 60Sn40Pb hypoeutectic solder*, http://spm.aif.ncsu.edu/papers/jeol.htm, 1997.

[26] DREYER, W., MÜLLER, W.H., *Computer Modeling of Micromorphological Change by Phase Field Models: Applications to Metals and Ceramics*, Journal of the Australasian Ceramic Society, 2000, 36 (1), pp. 83–94

[27] DREYER, W., MÜLLER, W.H., *Modeling Diffusional Coarsening in Eutectic Tin/Lead Solders: A Quantitative Approach*, Int. J. Sol. Struct., 2001, 38 (8), pp. 1433–1458.

[28] DREYER, W., *Development of microstructure based viscoplastic models for an advanced design of single crystal hot section components*, in: Development of Microstructural Based Viscoplastic Models for an Advanced Design of Single Crystal Hot Section Components (J. Olschewski, ed.), 1994, Brite/Euram Per. Prog. Rpt., pp. A.1-17-A.1–29.

[29] MÜLLER, W.H., *Mathematical vs. experimental stress analysis of inhomogeneities in solids*, Journal de Physique IV, Colloque C1, supplément au Journal de Physique III, 1996, 6, pp. C1-139–C1-148.

[30] MÜLLER, W.H., *Fourier transforms and their application to the formation of textures and changes of morphology in solids*, Proc. IUTAM Symp. on Transformation Problems in Composite and Active Materials, Cairo, Kluwer Academic Publishers, Dordrecht, Netherlands, 1998, pp. 61-72.

[31] CANUTO, C., HUSSAINI, M.Y., QUATERONI, A., ZANG, T.A., *Spectral methods in fluid dynamics*, Springer Series in Computational Physics. Springer Verlag, New York, 1988.

[32] MURA, T., *Micromechanics of Defects in Solids*, second revised edition, Martinus Nijhoff Publishers, Dordrecht, The Netherlands, 1987.

[33] MASSALSKI, T.B., *Structure of solid solutions*, in: Physical Metallurgy (edited by R.W. Cahn), North- Holland Publishing Company, Amsterdam, 1965.

[34] MTData, *NPL Databank for Materials Thermochemistry*, National Physical Laboratory, Queens Road, Teddington, Middlesex, TW11 0LW, 1998.

[35] DREYER, W., MÜLLER, W.H., OLSCHEWSKI, J., *An approximate analytical 2D-solution for the stresses and strains in eigenstrained cubic materials,* Acta Mechanica, 1999, 136 (3-4), pp. 171–192.

[36] MOULINEC, H., SUQUET, P., *A fast numerical method for computing the linear and nonlinear mechanical properties of composites*, C. R. Acad. Sci. Paris, 1994, 318 (II), pp. 1417–1423.

[37] MOULINEC, H., SUQUET, P., *A numerical method for computing the overall response of nonlinear composites with complex microstructure*, Comp. Meth. Appl. Mech. Engng., 1998, 157 (1-2), pp. 69–94.

[38] Brown, C.M., Dreyer, W., Müller, W.H., *Discrete Fourier transforms and their application to stress- strain problems in composite mechanics: A convergence study*, submitted to Proc. Royal Soc. A, 2000.

[39] Hawick, K.A., *Domain Growth in Alloys*, PhD- thesis, Edinburgh University, 1991.

[40] Larché F.C., Cahn J.W., *Phase changes in a thin plate with nonlocal self-stress effects*, Acta Metall. Mater., 1992. 40 (5), pp. 947–955.

[41] Wang, Y., Khachaturyan, A.G., *Shape instability during precipitate growth in coherent solids*, Acta metall. Mater., 1995, 43 (5), pp. 1837–1857.

[42] Li, D.Y., Chen, L.Q., *Computer simulation of morphological evolution and rafting of particles in Ni-based superalloys under applied stress*, Scripta Materialia, 1997, 37 (9), pp. 1271–1277.

[43] Koyama, T., Miyazaki, T., *Computer simulation of phase decomposition in two dimensions based on a discrete type non-linear diffusion equation*, Materials Transactions, JIM, 1998, 39 (1), pp. 169–178.

[44] Ghosh, G., Liu, Z.-K., *Modeling the atomic transport kinetics in high-lead solders*, Journal of Electronic Materials, 27 (12), pp. 1362–1366.

[45] Harris, P.G., Chaggar, K.S. and Whitmore, M.A., *The effect of ageing on the microstructure of 60:40 tin-lead solders*, Soldering and Surface Mount Technology, 1998, 7, 1991, pp. 20–23.